

Received 12 November 2023, accepted 5 December 2023, date of publication 7 December 2023, date of current version 13 December 2023.

Digital Object Identifier 10.1109/ACCESS.2023.3340731

## RESEARCH ARTICLE

# Numerical Simulations on AC Loss of the REBCO Tape Under Rotating Magnetic Field

YUAN WANG<sup>1,3</sup>, JIN FANG<sup>1</sup>, (Member, IEEE), YUSUKE SOGABE<sup>2</sup>, (Member, IEEE), RODNEY A. BADCOCK<sup>3</sup>, (Senior Member, IEEE), JAMES G. STOREY<sup>3</sup>, (Member, IEEE), AND ZHENAN JIANG<sup>3</sup>, (Senior Member, IEEE)

<sup>1</sup>School of Electrical Engineering, Beijing Jiaotong University, Beijing 100044, China

<sup>2</sup>Department of Electrical Engineering, Kyoto University, Kyoto 615-8510, Japan


<sup>3</sup>Paihau-Robinson Research Institute, Victoria University of Wellington, Wellington, Lower Hutt 5011, New Zealand

Corresponding authors: Zhenan Jiang (zhenan.jiang@vuw.ac.nz) and Jin Fang (jfang@bjtu.edu.cn)

This work was supported in part by the New Zealand Ministry of Business, Innovation and Employment under the Advanced Energy Technology Platform Program “High Power Electric Motors for Large Scale Transport” under Contract RTVU2004; in part by the Air Force Office of Scientific Research under Award FA2386-22-1-4054; and in part by the China Scholarship Council (CSC) and the CSC/Victoria University of Wellington Scholarship.

**ABSTRACT** REBCO coated conductors are exposed to rotating magnetic fields in various high-temperature superconducting (HTS) applications, such as HTS rotating machines and flux pumps. AC loss will be generated in the conductors when they carry AC current under rotating magnetic fields. We define AC loss in the coated conductors with and without current as total AC loss and magnetization loss, respectively. In this work, total AC loss and magnetization loss, in a REBCO tape under rotating magnetic fields and a perpendicular AC standing wave magnetic field are numerically investigated. We employ a 2D finite element method (FEM) based on the  $T$ - $A$  formulation, where  $T$  and  $A$ , are the current and magnetic vector potentials, respectively. In the simulations, the external magnetic field amplitude ( $B_m$ ) is up to 500 mT and the reduced AC current ( $i = I_t/I_{c0}$ ) varies from 0.1 to 0.9, where the  $I_t$  and  $I_{c0}$  are the amplitude of the transport current and self-field critical current of the conductor, respectively. Two different types of rotating fields are considered: one is a uniform field with equal amplitudes and phases at each position, and the other being a non-uniform field created by a rotating Halbach array. Different tape widths ranging from 4 mm to 40 mm are considered. Interestingly, the simulation results show substantially higher magnetization loss in the perpendicular standing wave compared to the rotating magnetic fields when  $B_m$  is over 100 mT. We attribute the result to the fact that the magnetization loss is proportional to  $J_c$  of the conductor at magnetic field amplitudes much greater than the effective penetration magnetic field. Evidently, the instantaneous loss curves of the SW model and RMF-Uniform model at 200 mT exhibited close similarity with evolving  $J_c$  values of the two models. Furthermore, when  $B_m$  is lower than the effective penetrated field, we observe a pronounced disparity in magnetization loss of the wider tape between uniform and non-uniform rotating fields. This highlights the importance of considering the effects of non-uniform field distribution, particularly at lower magnetic field. We further show that total AC loss under the perpendicular standing wave magnetic field remains greater than that under rotating magnetic fields when  $B_m > 100$  mT and  $i < 0.5$ .

**INDEX TERMS** REBCO coated conductors, rotating magnetic field, magnetization loss, total AC loss, finite element method (FEM).

The associate editor coordinating the review of this manuscript and approving it for publication was Agustin Leobardo Herrera-May .

## I. INTRODUCTION

The progress of high-temperature superconducting (HTS) coated conductors along with high efficiency and power

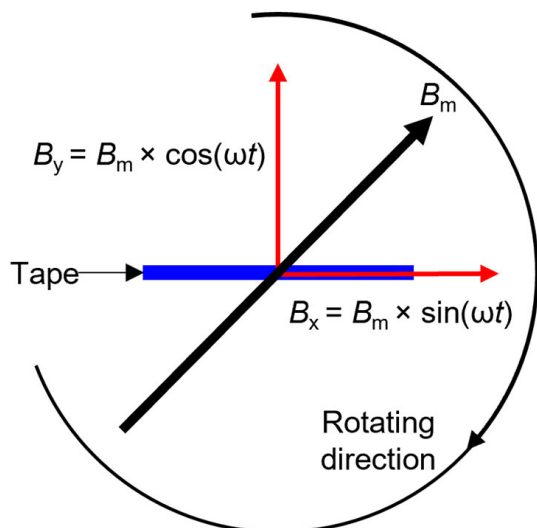


**FIGURE 1.** Characteristic of a rotating magnetic field. Here the rotating field has a constant amplitude value with  $B_m$  and its rotation direction is clockwise. The rotating field can be divided into two standing wave components with same amplitude and 90-degree phase shift. Relative to the tape position, these two standing wave components are perpendicular standing wave ( $B_y$ ) and parallel standing wave ( $B_x$ ) respectively, indicated by the red arrow lines.

density, has accelerated HTS machinery demonstrations for replacing their conventional counterparts in various areas, such as electric aircraft [1], [2], ship motors [3], [4] and wind turbines [5], [6]. However, among these applications, HTS conductors in the armature windings are exposed to a rotating magnetic field. As a result, AC loss will be generated in the armature windings, and it potentially poses a major challenge to the safe operation of the machine and its cooling system.

Until now, numerous studies have focused on the AC loss characteristics when HTS REBCO conductors are exposed to a perpendicular AC standing wave [7], [8], [9], [10], [11]. However, the magnetic field characteristics of perpendicular standing waves and rotating fields are different and previous conclusions for perpendicular standing wave magnetic fields may not be applicable to rotating fields. As shown in Fig. 1, a rotating field with constant magnetic field amplitude can be divided into the parallel standing wave magnetic field component ( $B_x$ ) and perpendicular standing wave magnetic field component ( $B_y$ ). These two standing wave magnetic field components exhibit identical magnetic amplitude with a 90-degree phase shift. The presence of the parallel standing wave magnetic field component potentially affects the behavior of AC loss in rotating fields. Therefore, it is necessary to explore the AC loss characteristics of HTS conductors in the rotating field environment.

A number of experimental and numerical studies have been conducted to investigate AC loss in a rotating field environment [7], [8], [9], [10], [11], [12], [13]. However, the predominant focus of these studies has been at the machine level, with only few papers considering rotating fields as an

isolated factor for fundamental research [14], [15], [16], [17]. In [14] and [15], both experimental results showed that AC loss in an HTS conductor under rotating fields is smaller than predicted by the Brandt-Indenbom (BI) equation [18], [19] at high applied magnetic field amplitudes. However, the authors did not provide reasons for this phenomenon or simply attributed it to the reduced critical current density ( $J_c$ ) at high magnetic field amplitudes. In [16], measured magnetization loss values of a Bi2223 tape under rotating fields and perpendicular standing wave magnetic fields were compared. Although the measured results exhibited good agreement, the magnetic field amplitudes were only up to 70 mT.

Until now, only one numerical work addressed AC loss in a rotating field [17]. The total AC loss of a vertical YBCO stack under both standing wave and rotating magnetic fields with transport current was compared. It is worth noting that rotating magnetic fields used in the numerical model is uniform, with the same phase and amplitude of magnetic field at each position. This is different from the non-uniform rotating fields found in real rotating machine environments. Moreover, the Kim model [20] used in the simulation is inadequate for capturing the complete information of angular magnetic field-dependent  $J_c$ .

In this paper, to address the research gap, the AC loss of a single REBCO tape under three different magnetic fields (standing wave, uniform rotating field and non-uniform rotating fields) have been simulated and compared, considering both scenarios with and without an AC current. The uniform and non-uniform rotating fields environment are achieved by applying two mutually vertical AC standing wave magnetic fields on the boundary and a rotating Halbach array, respectively in COMSOL Multiphysics, based on the  $T$ - $A$  formulation and  $E$ - $J$  power law. The three types of magnetic field models are named as the SW model, RMF-Uniform model, and RMF-Halbach model, respectively. The amplitude of the magnetic fields is up to 500 mT in this study, matching the field in some HTS rotating superconducting machines. For example, as indicated in [10], [21], and [22], the magnetic flux density in the air gap or the slot of the machines is around 500 mT. The reduced transport AC current ( $i = I_t/I_{c0}$ ) varies from 0.1 to 0.9, where the  $I_t$  and  $I_{c0}$  represent the amplitude of the transport current and self-field critical current of the conductor, respectively. The measured asymmetric field- and field-angle-dependent critical current data are applied to each case through the interpolation method. Finally, the simulation results are compared with BI equation and Norris equation [23]. To reveal AC loss characteristics of the tapes, the instantaneous loss,  $J_c$ , and their evolution over time or across the width of the tape have been considered.

## II. NUMERICAL MODELLING

### A. TWO TYPES OF ROTATING MAGNETIC FIELD

Fig. 2(a) depicts the schematic of RMF-Uniform model, in which every point is subjected to a uniform time-varying

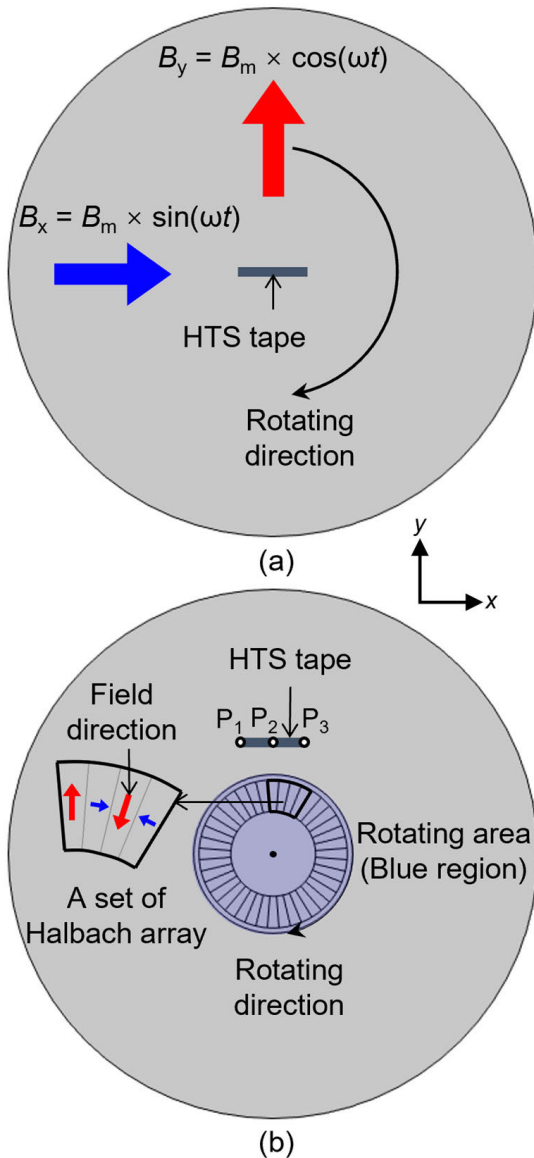


FIGURE 2. Schematics of the RMF-Uniform model (a) and RMF-Halbach model (b).

magnetic field with equal amplitude and phase. As shown in Fig. 1, combining two mutually vertical AC standing wave magnetic fields with same amplitude and frequency, but with a 90-degree phase difference, achieves a uniform rotating magnetic field. Here, a standing sine wave in the rightward direction (indicated by the blue arrow) and a standing cosine wave in the upward direction (indicated by the red arrow) have been applied. The resulting uniform rotating magnetic field rotates clockwise and its rotating frequency is 50 Hz.

Fig. 2(b) illustrates the schematic of the RMF-Halbach model. In contrast to the RMF-Uniform model, the magnetic field amplitude and phase in the RMF-Halbach model exhibits variation across different positions of the HTS tape. The non-uniform rotating field is achieved by a rotating

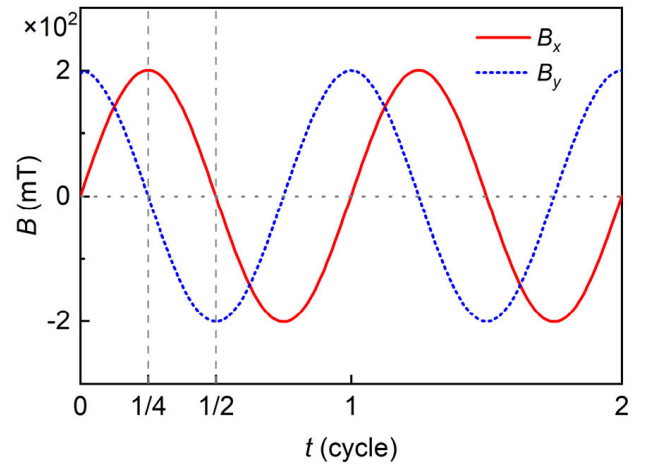


FIGURE 3. At the midpoint ( $P_2$ ),  $B_x$  and  $B_y$  components in the RMF-Halbach model vary over two rotating magnetic field cycles when HTS conductors have not been placed. The frequency of the rotating field is 50 Hz.

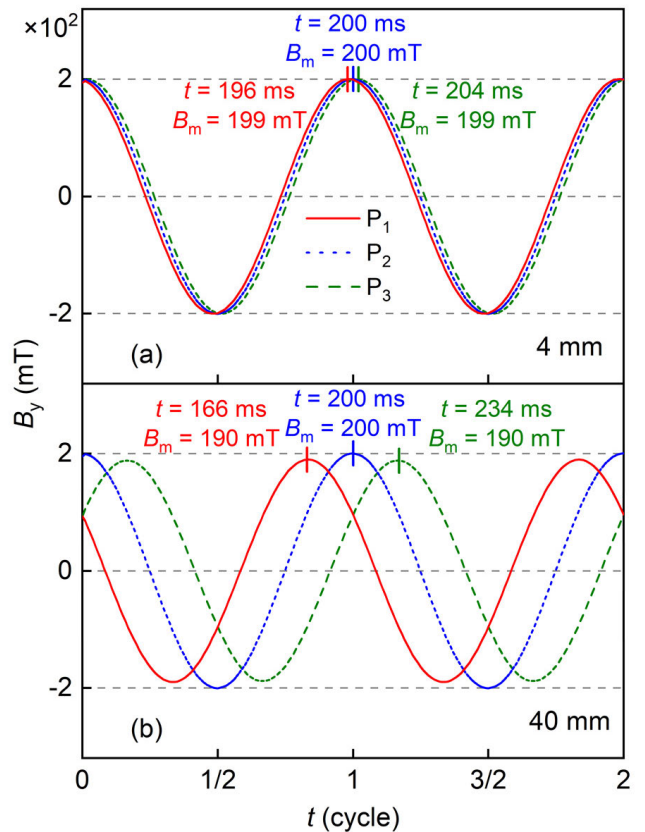


FIGURE 4. Time evolution of  $B_y$  components at  $P_1$ ,  $P_2$  and  $P_3$  (as shown in Fig. 2(b)) when HTS conductors have not been placed within a 4mm wide tape (a) and 40mm wide tape (b).

Halbach array consisting of 10 sets of permanent magnets. A set of the Halbach array is comprised of four permanent magnets with upward, rightward, downward, and leftward magnetic field direction respectively, as shown on the left side of Fig. 2(b). A moving mesh is utilized within the

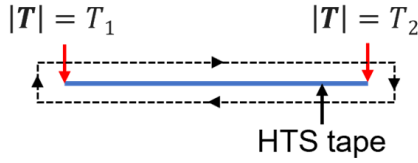


FIGURE 5. Boundary condition for the transport current in the HTS tape.

rotating area (indicated by the blue region in Fig. 2(b)) with a rotating frequency of 5 Hz, resulting in a rotating magnetic field frequency of 50 Hz. Its direction is set as clockwise. At the initial position, the magnet, facing the centre of the sample, produces an upward magnetic field. These settings are in accordance with the RMF-Uniform model. To observe the magnetic field distribution in the RMF-Halbach model, three points have been selected at the edges ( $P_1$ ,  $P_3$ ) and midpoint ( $P_2$ ) of the HTS tape area.

Fig. 3 plots the variations of the  $B_x$  and  $B_y$  components at  $P_2$  as a function of time. The  $B_y$  component exhibits a phase lag of one-quarter of a cycle compared to the  $B_x$  component, while maintaining the same amplitude and frequency. This is the same as the magnetic field distribution in the RMF-Uniform model.

Fig. 4 presents the  $B_y$  components at  $P_1$ ,  $P_2$ , and  $P_3$  as a function of time in one cycle, for both 4 mm and 40 mm tape widths when tapes have not been placed. In Fig. 4(a), for the 4 mm width, the amplitude almost remains constant at 200 mT at each point, and the peak time varies slightly, with a time lag of 4 ms. For the 40 mm width, as shown in Fig. 4(b), the amplitude at  $P_1$  and  $P_3$  is smaller at 190 mT compared to the  $P_2$  at 200 mT. The amplitude at  $P_1$  and  $P_3$  always have a 5% difference compared to that at  $P_2$  regardless of the magnetic field amplitude level. Additionally, there is a notable difference in the peak times, with a time lag of 34 ms.

### B. T-A FORMULATION

In the  $T$ - $A$  formulation [24], the current vector potential  $T$  is applied to the superconducting region and the magnetic vector potential  $A$  is applied in the whole model including the superconducting tape.  $T$  and  $A$  can be expressed in terms of the current density  $J$  and the magnetic flux density  $B$  as

$$J = \nabla \times T \quad (1)$$

$$B = \nabla \times A \quad (2)$$

The governing equations of the  $T$  formulation and the  $A$  formulation are

$$\nabla \times \rho \nabla \times T = -\frac{\partial B}{\partial t} \quad (3)$$

$$\nabla^2 A = -\mu_0 J \quad (4)$$

where  $\rho$  is the resistivity of the superconductor, and  $\mu_0$  is the vacuum permeability. Transport current is imposed by setting boundary conditions which can be written as

$$I = (T_1 - T_2) \delta \quad (5)$$

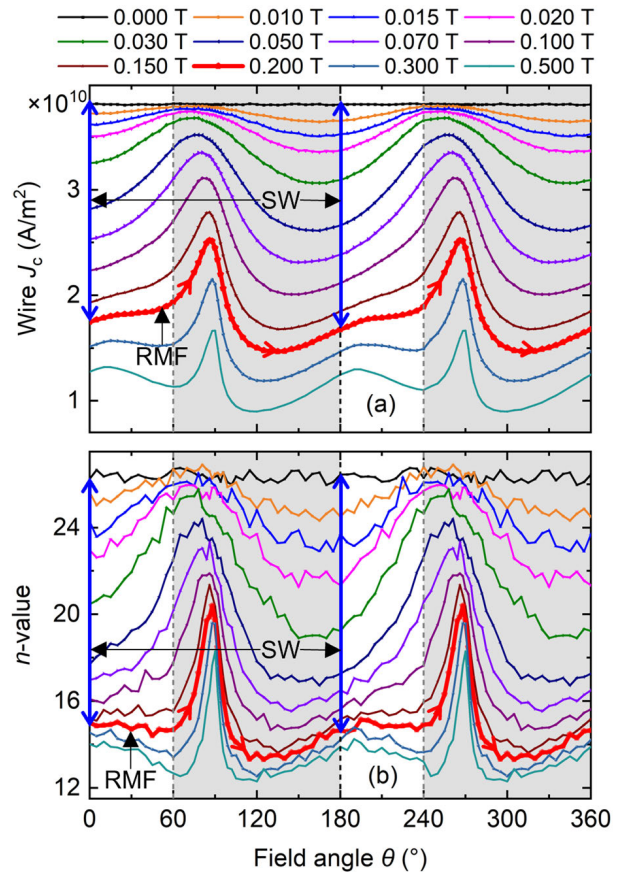


FIGURE 6. The measured  $J_c(B, \theta)$  &  $n(B, \theta)$  data used in the FEM. The data in the range  $240^\circ$  to  $360^\circ$  is extrapolated from the data in the range  $60^\circ$  to  $180^\circ$ . The red lines and their arrow indicates how the  $J_c$  and  $n$ -value varies with time when the tape under rotating fields of 200 mT, while the blue lines and their arrow indicate how the  $J_c$  and  $n$ -value changes with time when the tape is exposed to the standing wave of 200 mT.

where  $T_1$  and  $T_2$  are the values of  $T$  on the right and left edges as shown in Fig. 5, and  $\delta$  is the thickness of the HTS layer. The  $E$ - $J$  power law in Eq. (6) [25] is used in the FEM models for simulating the electromagnetic behaviour of the REBCO conductors.

$$\rho = \frac{E_c}{J_c(B, \theta)} \left| \frac{J_z}{J_c(B, \theta)} \right|^{n(B, \theta) - 1} \quad (6)$$

where  $E_c$  is the characteristic electric field  $1 \mu\text{V/cm}$ ,  $J_c(B, \theta)$  represents the critical current density of REBCO conductors, which depends on the magnetic field  $B$  and the field angle  $\theta$ , which is defined as the angle between the external magnetic field and the normal vector of the conductor wide-face. Similarly,  $n(B, \theta)$  denotes the power index, which is also depends on  $B$  and  $\theta$ .

SuperPower REBCO conductors (SCS4050) are considered for AC loss simulation. The specifications of the REBCO conductors are listed in Table 1. It is worth noting that the  $I_c$  of 40 mm HTS tape is scaled from the 4 mm tape.

Fig. 6(a) and Fig. 6(b) show the measured  $J_c(B, \theta)$  and  $n(B, \theta)$  of the conductors, respectively. The data are from

TABLE 1. Specifications of the REBCO coated conductor.

Parameters	Value
Tape width	4 / 40 mm
Strip thickness	0.18 mm
Superconducting layer thickness	1 μm
$J_c$ (self-field, 77K)	152 / 1520 A

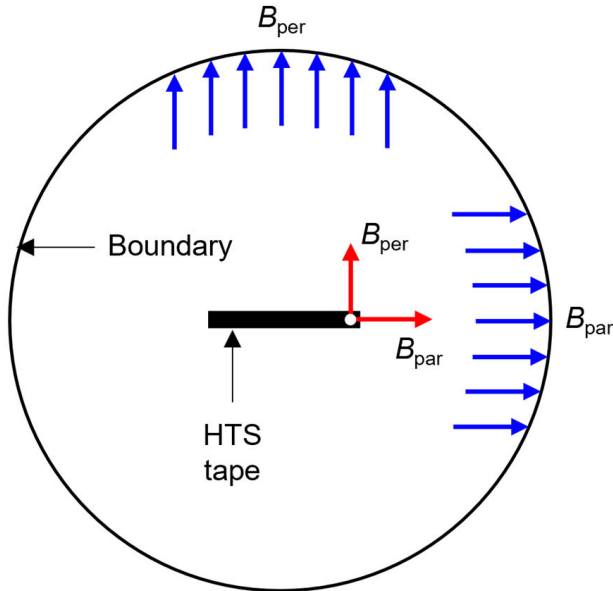


FIGURE 7. The two different definitions of  $B_{per}$  and  $B_{par}$  used for the interpolation look-up tables of  $J_c$  and  $n$ -value. Blue arrows represent the magnetic field components applied on the boundary; Red arrows represent the local magnetic field components on the HTS tape.

the high-temperature superconducting wire critical current database of Robinson Research Institute [26]. However, measured values only span the range from  $0^\circ$  to  $240^\circ$ . The remaining values, ranging from  $240^\circ$  to  $360^\circ$ , are extrapolated based on the data from  $60^\circ$  to  $180^\circ$  [10].

The modified Kim model [20], has been adopted to define the magnetic field dependence of the critical current dependence in some studies [27], [28]. However, compared with those modified Kim models, the direct interpolation method [29], [30] more fully considers the magnetic field- and field-angle-dependent critical current data. In our models, two three-column look-up interpolation tables, namely  $(B_{per}, B_{par}, J_c(B_{per}, B_{par}))$  and  $(B_{per}, B_{par}, n(B_{per}, B_{par}))$ , are used to define  $J_c(\mathbf{B}, \theta)$  and  $n(\mathbf{B}, \theta)$ . It is worth noting that in the SW and RMF-Uniform models,  $B_{per}$  and  $B_{par}$  represent the perpendicular and parallel magnetic field components applied to the boundary, respectively. This is depicted by the blue arrows in Fig. 7. For the SW model, the perpendicular and parallel magnetic field components applied on the boundary are:

$$B_{per} = B_m \times \cos(\omega t) \quad (7)$$

$$B_{par} = 0 \quad (8)$$

For the RMF-Uniform model, two components on the boundary can be written as:

$$B_{per} = B_m \times \sin(\omega t) \quad (9)$$

$$B_{par} = B_m \times \cos(\omega t) \quad (10)$$

where  $B_m$  is the magnetic field amplitude. However, for the RMF-Halbach model, where the magnetic field is created by permanent magnets,  $B_{per}$  and  $B_{par}$  are given by the perpendicular and parallel components at the midpoint  $P_2$  (see Fig. 2(b)) when tapes have not been placed.

In previous studies [10], [29],  $B_{per}$  and  $B_{par}$  were also given by the local perpendicular and parallel components on the HTS conductor, indicated by the red arrows in Fig. 7.

### III. SIMULATION RESULT AND DISCUSSION

#### A. MAGNETIZATION LOSS

Fig. 8 shows the simulated magnetization loss results plotted as a function of the magnetic field amplitude in the three models: SW-model, RMF-Uniform model and RMF-Halbach model. The analytical results from the Brandt-Indenbom (BI) equation for a superconducting strip under an AC perpendicular magnetic field [18] are included for reference. For the 4 mm-wide tape (see Fig. 8(a)), when the external magnetic field amplitude ( $B_m$ ) is below 100 mT, the magnetization loss values of all three cases agree well with each other and have good agreement with the analytical result. However, when  $B_m > 200$  mT, the loss values in all the three models become lower than the analytical values. This can be attributed to the decreased  $J_c$  caused by the influence of the external magnetic field. Meanwhile, it is worth noting that while the loss values of the two RMF models still show good agreement with each other, both exhibit lower values compared to the SW model. This discrepancy in magnetization loss can be attributed to the variation in  $J_c$  value distribution between the standing wave magnetic field and rotating magnetic fields. A more detailed discussion on this aspect is provided later in this section.

The general tendency of AC loss in the 40 mm-wide tape (as shown in Fig. 8 (b)) is similar to the 4 mm-wide tape. However, at  $B_m = 5, 10$  and 20 mT, the magnetization loss results of the two RMF models differ. This discrepancy in magnetization loss can be attributed to the variation of the magnetic field amplitude between the two RMF models. As mentioned in Section A of Chapter II, in the RMF-Halbach model, the difference in the amplitude between the edge and center points is equal regardless of the external magnetic field level. However, the different loss values are only observed at low magnetic field amplitudes. This observation can be explained using the BI equation [26]. According to the equation, the magnetization loss is proportional to  $B_m^4$  when  $B_m$  is much smaller than the effective magnetic field ( $B_p$ ), and proportional to  $B_m$  when  $B_m$  is much greater than  $B_p$  [31]. In current work,  $B_p$  for the 40 mm conductor is 37.5 mT as marked in Fig. 8(b). This implies that the magnetization loss is more sensitive to changes in  $B_m$  values when  $B_m$  is smaller than  $B_p$ . As shown in Fig. 4(b), the difference in  $B_m$  between

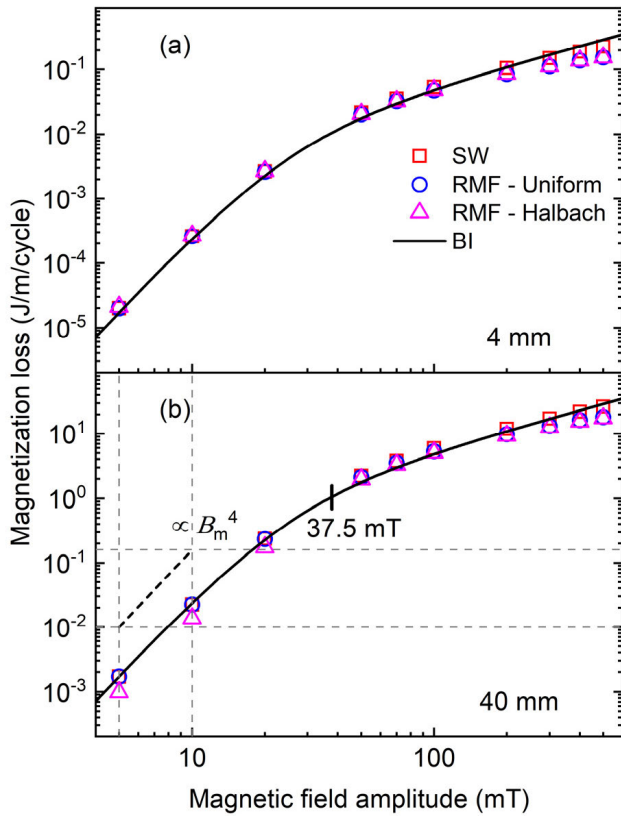


**FIGURE 8.** The magnetization loss as a function of magnetic field amplitude in the SW, RMF-Uniform, and RMF-Halbach models for different conductor widths: (a) 4 mm; (b) 40 mm. Analytical results from Brandt-Indenbom (BI) equation are included for reference.

$P_1$  and  $P_2$  for the RMF-Halbach model is 10 mT when  $B_m$  at  $P_2$  is 200 mT. The 5% difference in  $B_m$  values is the main cause of the difference in magnetization loss values at low magnetic fields.

In Fig. 9, the magnetization loss from the RMF-Uniform and RMF-Halbach models is plotted against the tape width, ranging from 4 mm to 40 mm, for 10 mT and 200 mT, respectively. In Fig. 9(a), at 10 mT, when the tape is not fully penetrated, the difference in loss between the two RMF models diverges as the conductor width increases. This is because the different positions of the wider conductors experience a greater difference in the magnetic field amplitudes than those in the narrower conductors. However, in Fig. 9(b), at 200 mT, when the tape is fully penetrated, the loss results from both models continue to agree with each other as the width increases because the magnetization loss is proportional to  $B_m^1$  at 200 mT.

Fig. 10(a) shows five moments in one cycle (at a frequency of 50 Hz) to observe the evolution of the normalized local current density ( $J_z/J_c$ ) in the two RMF models. As shown in Fig. 2, for the RMF-Uniform model,  $B_y$  represents the magnetic field in the y-direction applied at the boundary. For the RMF-Halbach model,  $B_y$  refers to the magnetic field component at  $P_2$  in the y-direction.

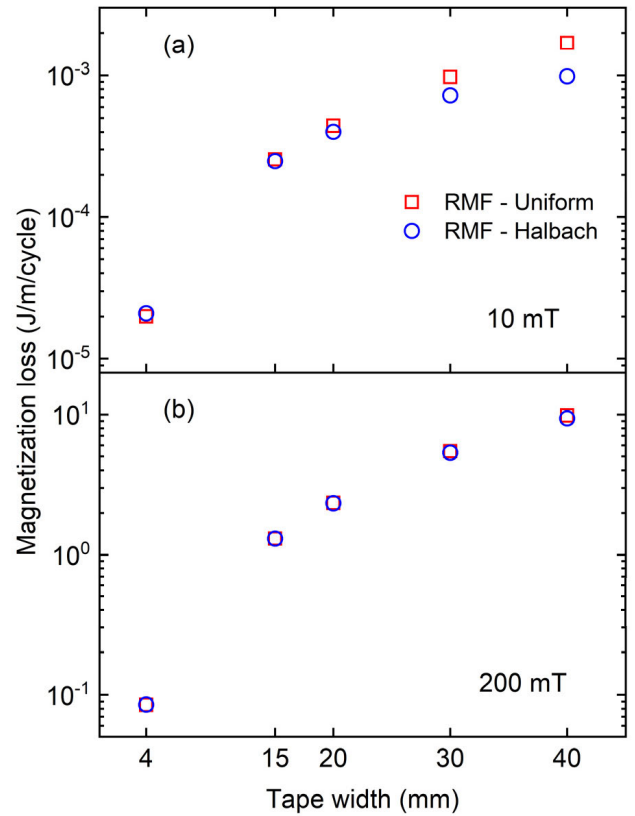
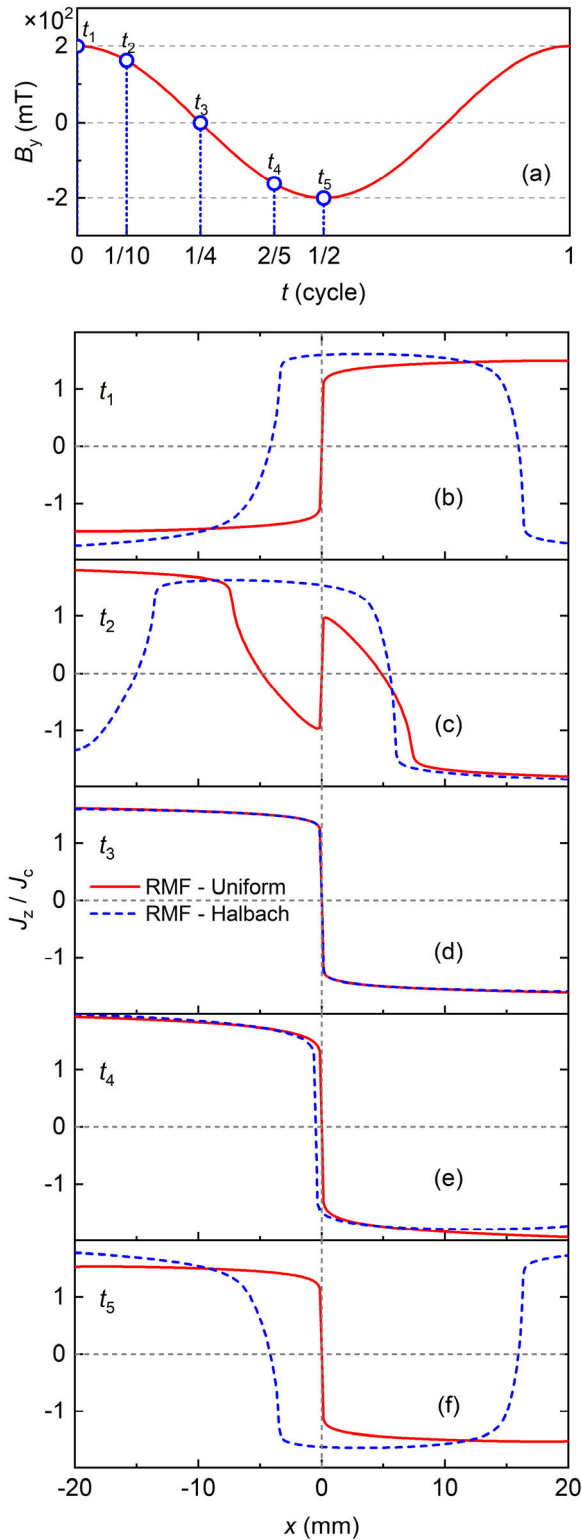


**FIGURE 9.** Magnetization loss from the RMF-Uniform and RMF-Halbach models as a function of tape width. (a) under 10 mT, (b) under 200 mT.

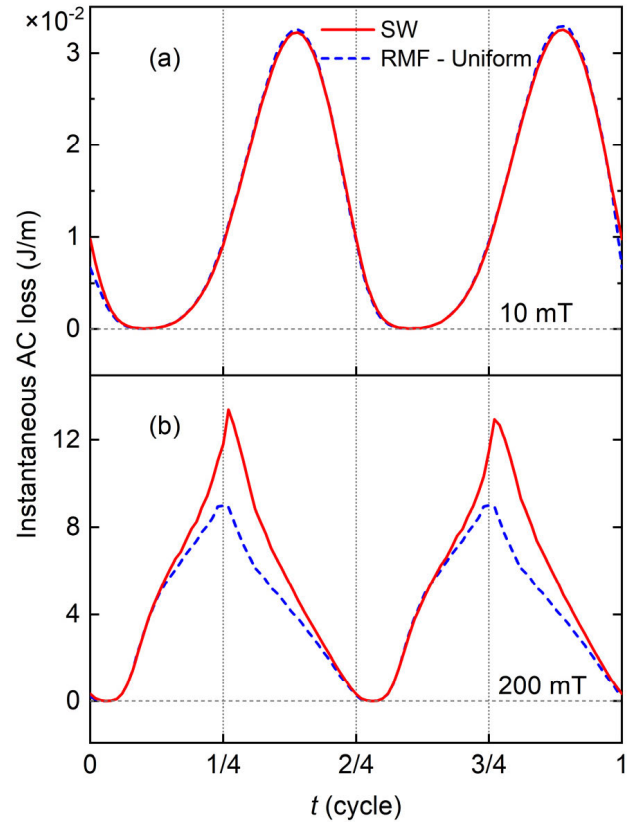
Fig. 10(b)-(f) presents the  $J_z/J_c$  distribution of the 40 mm-tape along the tape width between two RMF models at different moments, at 200 mT. The  $J_z/J_c$  distribution curves of the RMF-Uniform model exhibit central symmetry. However, the curves of the RMF-Halbach model are centrally asymmetric, except at  $t_3$  where the magnetic field distribution along the conductor width is axisymmetric. The asymmetric distribution is due to the phase shift of each position in the RMF-Halbach model shown in Fig. 4(b). Similar asymmetric  $J_z$  profiles were observed in the stator tape of an HTS flux pump by Matrira et al. where the stator tape in the flux pump is exposed to a revolving field generated by rotating rotor magnets [32]. It is worth noting that the asymmetric distributions have little effect on AC loss of the REBCO tape. The loss values from the RMF-Uniform and RMF-Halbach models remain identical at 200 mT, as shown in Fig. 8(b).

Fig. 11 compares the instantaneous AC loss between the SW model and RMF-Uniform model at 10 mT and 200 mT. As shown in Fig. 11(a), the instantaneous loss curves of the SW model and RMF-Uniform model agree well at 10 mT. However, at 200 mT, as shown in Fig. 11(b), the instantaneous loss curve of the RMF-Uniform model is lower than that of the SW model, and the greatest difference occurs near the 1/4 cycle and 3/4 cycle.

Fig 12 presents the  $J_c$  value of the RMF-Uniform and SW models over one field cycle at 200 mT. The  $J_c$  value of the



**FIGURE 10.** Comparison of the  $J_z/J_c$  distributions from the RMF-Uniform and RMF-Halbach models along a 40mm tape, at 200 mT. Plot (a) shows  $B_y$  during one cycle at a frequency of 50Hz. Corresponding to Fig.2, in the RMF-Uniform model,  $B_y$  refers to its applied magnetic field in the y-direction. In the RMF-Halbach model,  $B_y$  refers to the y-direction magnetic field of  $P_2$ . Plots (b)-(e) show the  $J_z/J_c$  distribution at five moments.



**FIGURE 11.** Comparison of the instantaneous AC loss change with time between the SW model and RMF-Uniform model. (a) 10 mT, (b) 200mT.

RMF-Uniform model is lower than that of the SW model for most of the time, and the greatest difference occurs near 1/4 and 3/4 cycles as well. Interestingly, comparing Fig. 12 with Fig. 11(b), the instantaneous loss curves demonstrate a similar trend with the  $J_c$  curves. We attribute this to the behavior of magnetization loss which is proportional to the critical current  $J_c$  when the magnetic field is much greater than  $B_p$  [18].

The key reason for the difference in  $J_c$  distributions in Fig. 12 from the two models comes from the different magnetic field characteristics of the RMF-uniform model and the standing wave in the SW model. For the RMF-uniform model, its magnetic field amplitude remains constant at 200 mT, while its field angle changes with time. The evolution of its  $J_c$  values corresponds to the red line in Fig. 6(a). Conversely, for the SW model, its amplitude varies with time from 0 to 200 mT, while its field angle remains fixed at  $0^\circ$  ( $360^\circ$ ) or  $180^\circ$  degrees. The evolution of its  $J_c$  values corresponds to the blue line in Fig. 6(a). Apparently, the SW model has much higher  $J_c$  values than the RMF-Uniform model for the majority of the time. The difference in  $J_c$  profiles over time for the two models is the single most important reason which causes the difference in loss values between the two models at high magnetic field amplitudes.

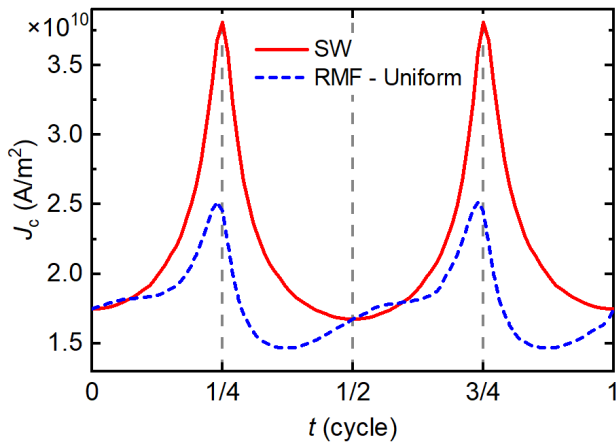


**FIGURE 12.** Comparison of  $J_c$  changes over one cycle at a frequency of 50Hz between the SW and RMF-Uniform models under 200 mT.

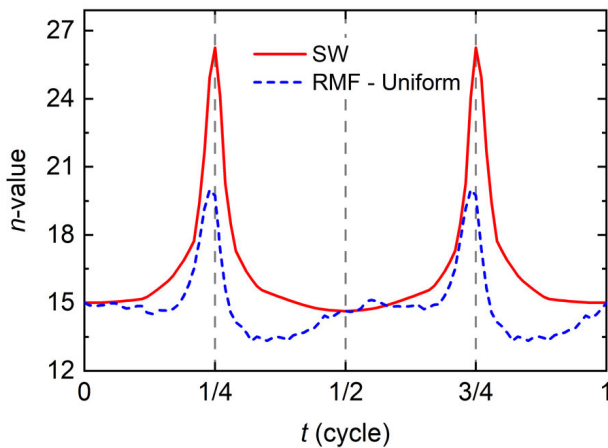


**FIGURE 13.** Comparison of  $n$ -value changes over one cycle at a frequency of 50Hz between the SW and RMF-Uniform models under 200 mT.

Fig. 13 presents the evolution of  $n$ -values from the RMF-Uniform and SW models over one field cycle at 200 mT. Similar to the  $J_c$  distributions in Fig. 12, the  $n$ -value of the RMF-Uniform model is lower than that of the SW model for most of the time. In Fig. 6(b), the evolutions of  $n$ -value in RMF-Uniform model and SW model at 200 mT are indicated by the red line and blue line, respectively.

The differences in  $J_c$  and  $n$  values between the RMF-Uniform model and SW model not only contribute to the disparities in losses but also result in variations in other electromagnetic variables. To further probe the loss difference in the RMF-Uniform model and SW model at high magnetic fields, Fig. 14 shows simulation results of  $J_z/J_c$ ,  $J_z$ ,  $E$ ,  $P$  distributions across the 4 mm-wide tape from the SW and RMF-Uniform models at 200 mT at 1/4 cycle, where  $J_z/J_c$  is the normalized local current density,  $P$  is the instantaneous power. Between the two models, all properties exhibit disagreement (see Fig. 14 (a)-(e)), which can be attributed to the variation in  $J_c$  and  $n$  values. Fig. 14(a) shows that the  $|J_z/J_c|$  values of the RMF-Uniform model are

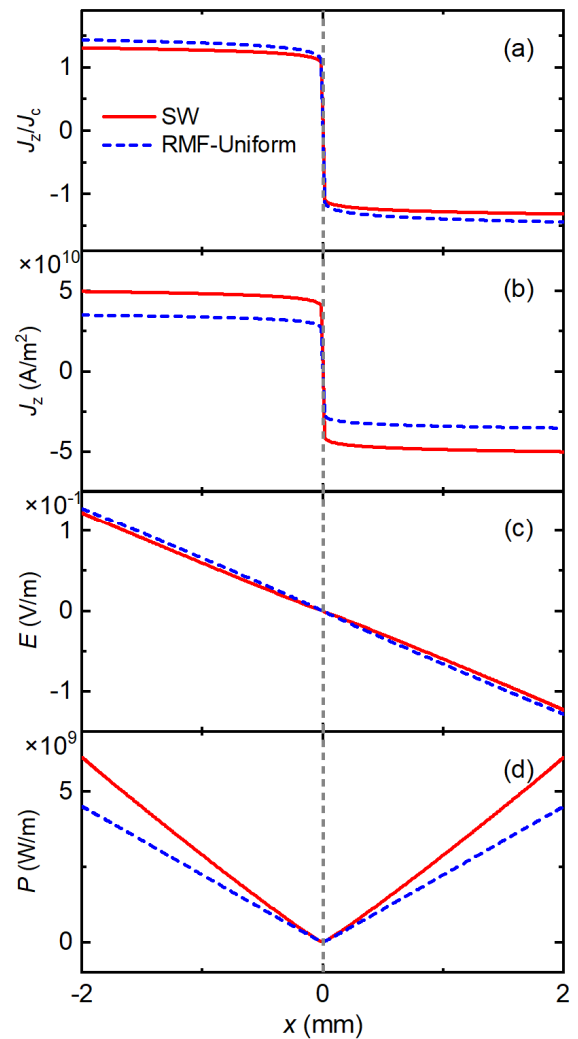


**FIGURE 14.** Simulated change in electromagnetic variables along a 4mm sample width for the SW and RMF-Uniform models at 1/4 cycle under 200mT. From (a) to (d) are the normalized local current density,  $J_z/J_c$ , the local current density,  $J_z$ , the electric field,  $E$ , and the instantaneous power density,  $P$ .

larger than those of the SW model. This is due to the smaller  $n$ -value of the RMF-Uniform model than that of the SW model. At 1/4 cycle, as shown in Fig. 13, the  $n$ -value of the RMF-Uniform model is 19.73, while that of the SW model is 26.25. The different  $n$ -value also contributes to a difference in  $E$  distribution, as shown in Fig. 14(c), where  $E$  of the RMF-Uniform model is slightly greater than that of the SW model. Fig. 14(b) shows that  $J_z$  values in the RMF-Uniform model is smaller than those of the SW model at 1/4 cycle. This discrepancy arises from the fact that  $J_c$  in the RMF-Uniform model, with a value of  $2.52 \times 10^{10}$  A/m<sup>2</sup>, is smaller than that in the SW model, which has a value of  $3.67 \times 10^{10}$  A/m<sup>2</sup>, as shown in Fig. 12. Finally, as shown in Fig. 14(d),  $P$  in the SW model is greater than that of the RMF-Uniform model. This is mainly due to the larger  $J_z$  in the SW model, although  $E$  is slightly smaller than that in the SW model.



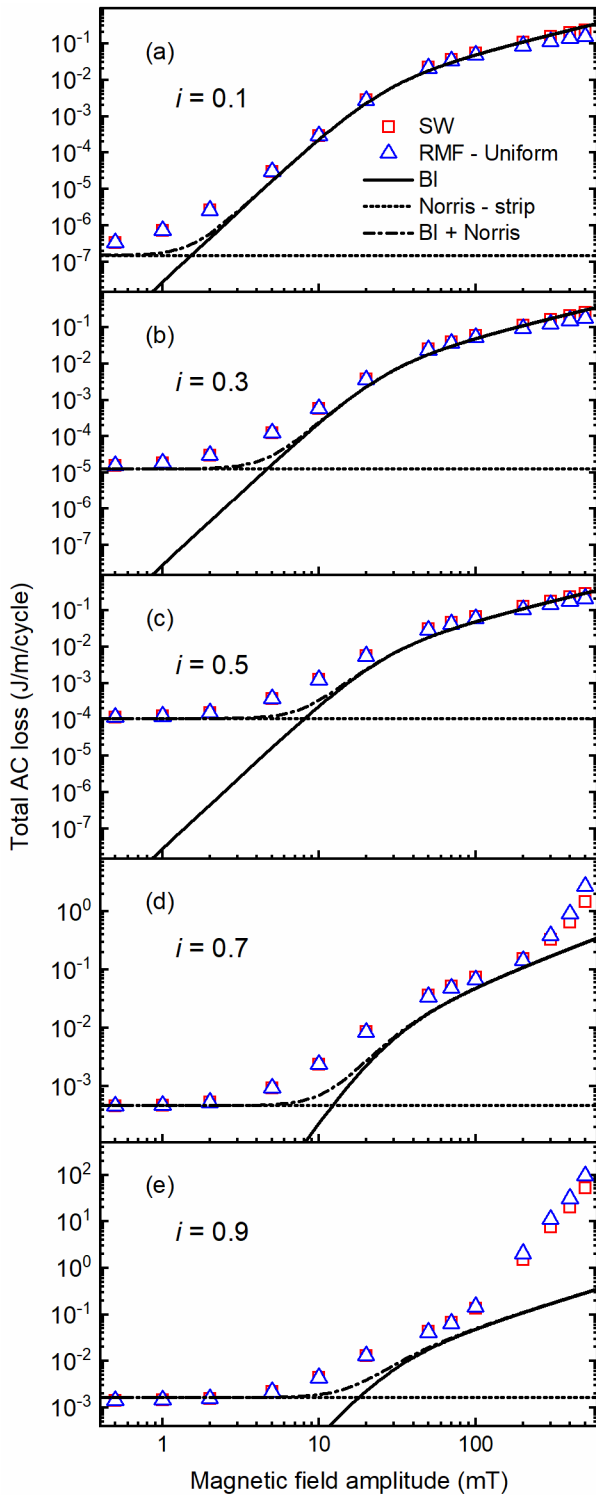


**FIGURE 15.** The total AC loss of a single tape as a function of the external AC magnetic field amplitude for five different reduced current levels,  $i$ . BI, Norris and BI + Norris theoretical values curves have been added for reference.

**B. TOTAL AC LOSS**

Fig. 15 shows the simulated total AC loss curves of the 4 mm-wide tape plotted as a function of the external AC

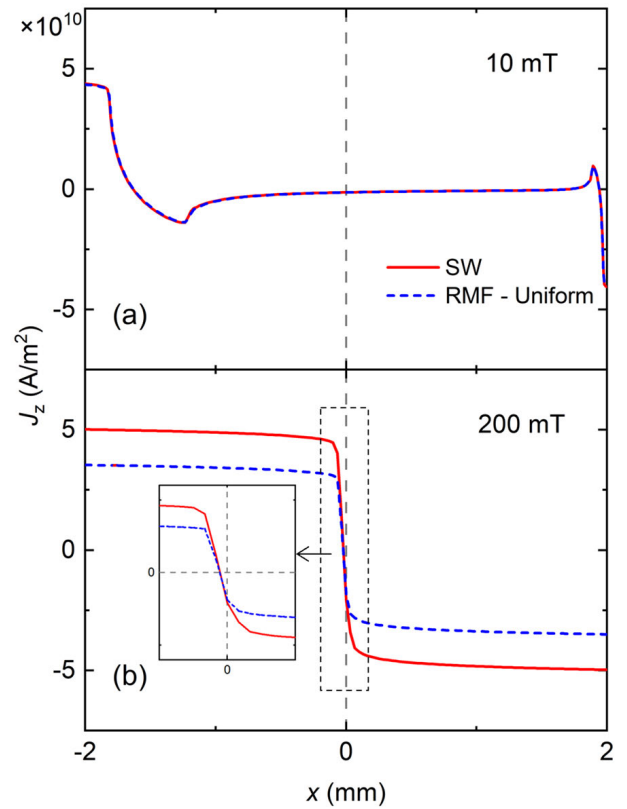


**FIGURE 16.** The local current density ( $J_z$ ) of the SW model and RMF-Halbach model along the tape width, at 25 ms (1/4 cycle), when  $i = 0.3$ . The inset shows the center part of figure 16(b).

magnetic field amplitude for five different reduced current levels,  $i$  ( $I_t / I_{c0}$ ), where the  $I_t$  and  $I_{c0}$  are the amplitude of the transport current and self-field critical current of the conductor, respectively. The phase of the current has been chosen to be the same as that of the external magnetic field, although there will be a phase difference in practical rotating machines. The analytical data from BI equation for the strip under the perpendicular field and Norris strip equations [23] are plotted together as reference.

For  $i = 0.3$ , and  $0.5$ , as shown in Fig. 15 (b) and (c), the total AC loss values can be characterized by three stages. Stage one: when the external field amplitude is below 1 mT, the total AC loss agrees with the Norris-strip value. This is because transport loss dominates the total AC loss at this stage, as indicated by the good agreement between Norris-strip value and “BI + Norris” value. Stage two: within the amplitude range between 2 mT - 70 mT for  $i = 0.3$  and between 5 mT - 100 mT for  $i = 0.5$ , the total AC loss value surpasses the “BI + Norris” curve. This result can be attributed to the interaction between the AC external magnetic field and current: transport loss increases with increasing external magnetic field, and the magnetization loss increases with increasing AC transport current [33]. Stage three: when the external field amplitude is over 100 mT, the total AC loss values agree with the BI curve. This is due to the dominance of the magnetization loss in the

total AC loss. It is worth noting that when  $i = 0.1$ , there is no ‘stage one’ due to the transport current being too small to dominate the total AC loss even at 0.5 mT. When  $i = 0.7$  and 0.9, there is no ‘stage three’. This is because the transport current is significantly higher than  $J_c$  at high magnetic field amplitudes, resulting in  $J_z/J_c$  much greater than 1 and hence flux flow loss [34].

The total AC loss values between the SW and RMF-Uniform models agree with one another when the magnetic field amplitude is lower than 100 mT. However, above 100 mT, there is a notable difference between the loss values of the two models. When  $i$  is lower than 0.5 (as seen in Fig. 15(a), (b), (c)), the total AC loss values of the SW model surpass those of the RMF-Uniform model. As mentioned earlier, the magnetization loss dominates the total AC loss and there is difference in magnetization loss values when  $B_m > 100$  mT. On the other hand, for  $i > 0.5$  (as seen in Fig. 15(d), (e)) and  $B_m > 100$  mT, the total AC loss in the SW model becomes smaller than that of the RMF-Uniform model. In the region where flux flow is the main loss mechanism, the loss is inversely proportional to  $J_c$ . As shown in Fig. 12,  $J_c$  of the SW model is larger than that of rotating fields, resulting in the AC loss of SW model being smaller than that of RMF-Uniform model.

Fig. 16 presents  $J_z$  distributions of the SW and RMF-Uniform models along the tape width at 10 mT and 100 mT, when  $i = 0.3$  at 25 ms (1/4 cycle). At 10 mT (see Fig. 16(a)), the  $J_z$  distributions of both models agree. On the contrary, at 200 mT (see Fig. 16(b)),  $J_z$  values between the two models differ. These observations are similar to the  $J_c$  distributions shown in Fig. 14. However, unlike Fig. 14, the  $J_z$  distributions shown in Fig. 16 are not centrally symmetric. This is due to the superposition of the shielding currents and transport current, which strengthen current on one edge while weakening it on the other edge.

#### IV. CONCLUSION

This study presents the simulation of magnetization loss (without current) and total AC loss (with AC current) in a single REBCO tape under three types of magnetic fields: a perpendicular AC standing wave (SW model), a uniform rotating field (RMF-Uniform model) and a non-uniform rotating field (RMF-Halbach model). The amplitude of external magnetic field ( $B_m$ ) is up to 500 mT and the reduced current ( $i$ ) ranges from 0 to 0.9.

For  $B_m < 100$  mT, the simulated magnetization loss values of the 4 mm REBCO conductor between the SW model and two RMF models agree well with each other and with the analytical values from the Brandt-Indenbom (BI) equation. However, when  $B_m > 100$  mT, the magnetization loss in the SW model is noticeably higher than those of the RMF models. This is mainly due to the magnetization loss being proportional to  $J_c$  of the conductor for magnetic field amplitudes much greater than the effective penetration field. Evidently, the instantaneous loss curves of the SW and RMF-Uniform models at 200 mT exhibited close similarity with the evol-

ving  $J_c$  values of the two models. Notably, in the  $J_c$  curves at 200 mT plotted as a function of the field angle, for majority of the time, the SW model showed much higher  $J_c$  values than those of the RMF-Uniform model which vary with the field angle at 200 mT. Furthermore, the biggest difference of the  $J_c$  values occurs near the 1/4 and 3/4 cycles.

Obvious differences in the magnetization loss values between the RMF-Uniform model and RMF-Halbach model were observed for the 40 mm-wide tape when  $B_m < 37.5$  mT (the effective penetrated field). The difference becomes greater with increasing tape width. We attribute the difference to the non-uniform magnetic field distribution at different positions of the conductor in the RMF-Halbach model.

The simulated total AC loss values of the SW and RMF-Uniform models for the 4 mm-tape agree well with each other for  $B_m < 100$  mT regardless of the amplitude of the transport current, and the values are greater than ‘BI + Norris’ values due to the interaction between the external field and transport current except very low magnetic field amplitudes. When  $B_m > 100$  mT, for  $i < 0.5$ , the total AC loss values in the SW model are greater than those in the RMF-Uniform model, and both values are close to the values from BI equation. The result implies that the total AC loss in a coated conductor under rotating magnetic fields with high magnetic field amplitudes can be predicted by the BI equation.

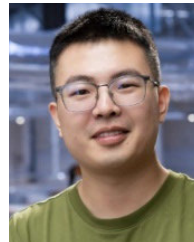
#### ACKNOWLEDGMENT

All data is provided in full in the results section of this article.

#### REFERENCES

- [1] F. Grilli, “Superconducting motors for aircraft propulsion: The advanced superconducting motor experimental demonstrator project,” *J. Phys., Conf. Ser.*, vol. 1590, no. 1, Jul. 2020, Art. no. 012051.
- [2] M. Filipenko, L. Kühn, T. Gleixner, M. Thummet, M. Lessmann, D. Möller, M. Böhm, A. Schröter, K. Häse, J. Grundmann, M. Wilke, M. Frank, P. V. Hasselt, J. Richter, M. Herranz-Garcia, C. Weidemann, A. Spangolo, M. Klöpzig, P. Gröppel, and S. Moldenhauer, “Concept design of a high power superconducting generator for future hybrid-electric aircraft,” *Superconductor Sci. Technol.*, vol. 33, no. 5, Mar. 2020, Art. no. 054002.
- [3] W. Li, T. W. Ching, K. T. Chau, and C. H. T. Lee, “A superconducting Vernier motor for electric ship propulsion,” *IEEE Trans. Appl. Supercond.*, vol. 28, no. 3, pp. 1–6, Apr. 2018.
- [4] T. Yanamoto, M. Izumi, K. Umemoto, T. Oryu, Y. Murase, and M. Kawamura, “Load test of 3-MW HTS motor for ship propulsion,” *IEEE Trans. Appl. Supercond.*, vol. 27, no. 8, pp. 1–5, Dec. 2017.
- [5] X. Song, C. Bühner, P. Brutsaert, J. Krause, A. Ammar, J. Wieszorek, J. Hansen, A. V. Rebsdorf, M. Dhallo, A. Bergen, T. Winkler, S. Wessel, M. T. Brake, J. Kellers, H. Pütz, M. Bauer, H. Kyling, H. Boy, and E. Seitz, “Designing and basic experimental validation of the world’s first MW-class direct-drive superconducting wind turbine generator,” *IEEE Trans. Energy Convers.*, vol. 34, no. 4, pp. 2218–2225, Dec. 2019.
- [6] I. Marino, A. Pujana, G. Sarmiento, S. Sanz, J. M. Merino, M. Tropeano, J. Sun, and T. Canosa, “Lightweight MgB<sub>2</sub> superconducting 10 MW wind generator,” *Superconductor Sci. Technol.*, vol. 29, no. 2, Dec. 2015, Art. no. 024005.
- [7] C. R. Vargas-Llanos, S. Lengsfeld, and F. Grilli, “T-A formulation for the design and AC loss calculation of a superconducting generator for a 10 MW wind turbine,” *IEEE Access*, vol. 8, pp. 208767–208778, 2020.

- [8] Y. Yang, H. Yong, X. Zhang, and Y. Zhou, "Numerical simulation of superconducting generator based on the T-A formulation," *IEEE Trans. Appl. Supercond.*, vol. 30, no. 8, pp. 1–11, Dec. 2020.
- [9] Y. Liu, J. Ou, Y. Cheng, F. Schreiner, Y. Zhang, C. Vargas-Llanos, F. Grilli, R. Qu, M. Doppelbauer, and M. Noe, "Investigation of AC loss of superconducting field coils in a double-stator superconducting flux modulation generator by using T-A formulation based finite element method," *Superconductor Sci. Technol.*, vol. 34, no. 5, Apr. 2021, Art. no. 055009.
- [10] S. You, S. S. Kalsi, M. D. Ainslie, R. A. Badcock, N. J. Long, and Z. Jiang, "Simulation of AC loss in the armature windings of a 100 kW all-HTS motor with various (RE)BCO conductor considerations," *IEEE Access*, vol. 9, pp. 130968–130980, 2021.
- [11] S. You, S. S. Kalsi, M. D. Ainslie, R. A. Badcock, N. J. Long, and Z. Jiang, "Numerical simulation of AC loss in the armature windings of two 50 kw-class all-HTS motors with different pole shapes," *IEEE Trans. Appl. Supercond.*, vol. 32, no. 4, pp. 1–7, Jun. 2022.
- [12] Y. Zhang, Y. Cheng, R. Qu, D. Li, Y. Gao, and Q. Wang, "AC loss analysis and modular cryostat design of a 10-MW high-temperature superconducting double stator flux modulation machine," *IEEE Trans. Ind. Appl.*, vol. 58, no. 6, pp. 7153–7162, Nov. 2022.
- [13] X. Zhou, S. Zou, W. Chen, S. Song, Z. Chen, J. Xu, and M. Yan, "Conceptual design, AC loss calculation, and optimization of an airborne fully high temperature superconducting generator," *Phys. C, Supercond. Its Appl.*, vol. 605, Feb. 2023, Art. no. 1354207.
- [14] P. K. Ghoshal, T. A. Coombs, and A. M. Campbell, "Calorimetric method of AC loss measurement in a rotating magnetic field," *Rev. Sci. Instrum.*, vol. 81, no. 7, Jul. 2010, Art. no. 074702.
- [15] J. P. Murphy, N. N. Gheorghiu, T. Bullard, T. Haugan, M. D. Sumpston, M. Majoros, and E. W. Collings, "AC loss in YBCO coated conductors at high dB/dt measured using a spinning magnet calorimeter (stator testbed environment)," *Cryogenics*, vol. 86, pp. 57–69, Sep. 2017.
- [16] J. Ogawa, S. Fukui, T. Oka, Y. Sano, M. Ogawa, and S. T. Ranecky, "Experimental investigation of AC loss characteristics in HTS tape with rotating magnetic field," *IEEE Trans. Appl. Supercond.*, vol. 27, no. 4, pp. 1–4, Jun. 2017.
- [17] W. A. Soomro, Y. Guo, H. Lu, J. Zhu, J. Jin, and B. Shen, "Three-dimensional numerical characterization of high-temperature superconductor bulks subjected to rotating magnetic fields," *Energies*, vol. 15, no. 9, p. 3186, Apr. 2022.
- [18] E. H. Brandt and M. Indenbom, "Type-II-superconductor strip with current in a perpendicular magnetic field," *Phys. Rev. B, Condens. Matter*, vol. 48, no. 17, pp. 12893–12906, Nov. 1993.
- [19] Z. Jiang, N. Amemiya, O. Maruyama, and Y. Shiohara, "Critical current density distribution and magnetization loss in YBCO coated conductors," *Phys. C, Supercond. Appl.*, vols. 463–465, pp. 790–794, Oct. 2007.
- [20] Y. B. Kim, C. F. Hempstead, and A. R. Strnad, "Critical persistent currents in hard superconductors," *Phys. Rev. Lett.*, vol. 9, no. 7, pp. 306–309, Oct. 1962.
- [21] M. Zhang, F. Eastham, and W. Yuan, "Design and modeling of 2G HTS armature winding for electric aircraft propulsion applications," *IEEE Trans. Appl. Supercond.*, vol. 26, no. 3, pp. 1–5, Apr. 2016.
- [22] S. S. Kalsi, R. A. Badcock, J. G. Storey, K. A. Hamilton, and Z. Jiang, "Motors employing REBCO CORC and MgB<sub>2</sub> superconductors for AC stator windings," *IEEE Trans. Appl. Supercond.*, vol. 31, no. 9, pp. 1–7, Dec. 2021.
- [23] W. T. Norris, "Calculation of hysteresis losses in hard superconductors carrying AC: Isolated conductors and edges of thin sheets," *J. Phys. D, Appl. Phys.*, vol. 3, no. 4, pp. 489–507, Apr. 1970.
- [24] H. Zhang, M. Zhang, and W. Yuan, "An efficient 3D finite element method model based on the T-A formulation for superconducting coated conductors," *Superconductor Sci. Technol.*, vol. 30, no. 2, Feb. 2017, Art. no. 024005.
- [25] J. Rhyner, "Magnetic properties and AC-losses of superconductors with power law current—Voltage characteristics," *Phys. C, Supercond.*, vol. 212, nos. 3–4, pp. 292–300, Jul. 1993.
- [26] S. C. Wimbush and N. M. Strickland, "A public database of high-temperature superconductor critical current data," *IEEE Trans. Appl. Supercond.*, vol. 27, no. 4, pp. 1–5, Jun. 2017.
- [27] L. Rostila, J. Lehtonen, R. Mikkonen, J. Šouc, E. Seiler, T. Melišek, and M. Vojenčiak, "How to determine critical current density in YBCO tapes from voltage-current measurements at low magnetic fields," *Superconductor Sci. Technol.*, vol. 20, no. 12, pp. 1097–1100, Sep. 2007.
- [28] E. Pardo, M. Vojenčiak, F. Gömöry, and J. Šouc, "Low-magnetic-field dependence and anisotropy of the critical current density in coated conductors," *Superconductor Sci. Technol.*, vol. 24, no. 6, Apr. 2011, Art. no. 065007.
- [29] Z. Jiang, N. Endo, S. C. Wimbush, J. Brooks, W. Song, R. A. Badcock, D. Miyagi, and M. Tsuda, "Exploiting asymmetric wire critical current for the reduction of AC loss in HTS coil windings," *J. Phys. Commun.*, vol. 3, no. 9, Sep. 2019, Art. no. 095017.
- [30] D. Hu, M. D. Ainslie, M. J. Raine, D. P. Hampshire, and J. Zou, "Modeling and comparison of in-field critical current density anisotropy in high-temperature superconducting (HTS) coated conductors," *IEEE Trans. Appl. Supercond.*, vol. 26, no. 3, pp. 1–6, Apr. 2016.
- [31] Y. Sun, J. Fang, A. E. Pantoja, R. A. Badcock, N. J. Long, and Z. Jiang, "Role of asymmetric critical current on magnetization loss characteristics of (RE)Ba<sub>2</sub>Cu<sub>3</sub>O<sub>7-d</sub> coated conductors at various temperatures," *J. Appl. Phys.*, vol. 130, no. 8, Aug. 2021, Art. no. 083902.
- [32] R. C. Mataira, M. D. Ainslie, R. A. Badcock, and C. W. Bumby, "Origin of the DC output voltage from a high-*t<sub>c</sub>* superconducting dynamo," *Appl. Phys. Lett.*, vol. 114, no. 16, Apr. 2019, Art. no. 162601.
- [33] N. Amemiya, Z. Jiang, Y. Iijima, K. Kakimoto, and T. Saitoh, "Total AC loss of YBCO coated conductor carrying AC transport current in AC transverse magnetic field with various orientations," *Superconductor Sci. Technol.*, vol. 17, no. 8, pp. 983–988, Jun. 2004.
- [34] Z. Jiang, N. Amemiya, M. Nakahata, Y. Iijima, K. Kakimoto, T. Saitoh, and Y. Shiohara, "AC loss characteristics of YBCO coated conductors with varying magnitude of critical current," *IEEE Trans. Appl. Supercond.*, vol. 16, no. 2, pp. 85–88, Jun. 2006.



**YUAN WANG** received the M.Eng. degree in electrical engineering from Beijing Jiaotong University, Beijing, China, in 2019, where he is currently pursuing the Ph.D. degree. In November 2022, he joined the Robinson Research Institute, Victoria University of Wellington, New Zealand, as a joint Ph.D. degree student between Beijing Jiaotong University and the Victoria University of Wellington. His current research interest includes the AC loss characterization of high-temperature superconducting (HTS) material under a rotating magnetic field environment.



**JIN FANG** (Member, IEEE) received the Ph.D. degree from the Institute of Plasmas, Chinese Academy of Sciences, in 2002. His major is condensed matter physics. In 2002, he joined the Department of Physics, Tsinghua University, for postdoctoral research, and mainly engaged in basic application research of high temperature superconducting tapes. In 2004, he joined Beijing Jiaotong University, to do research on power transmission cables, superconducting magnetic levitation technology, superconducting linear motors, and power system simulation. He has published more than 100 papers on superconductivity, including more than 50 SCI papers. His five patents have been awarded for the invention of HTS linear induction motors. His research interests include design, stability and AC losses of superconducting materials, cables, and superconducting magnets. He was awarded a NZ Catalyst Leaders funding of the Royal Society of New Zealand (2018–2021).



**YUSUKE SOGABE** (Member, IEEE) received the B.Eng. degree from the Undergraduate School of Electrical and Electronic Engineering, Kyoto University, Japan, in 2014, and the M.Eng. and Ph.D.-Eng. degrees from the Department of Electrical Engineering, Kyoto University, in 2016 and 2019, respectively.

He joined the Applied Superconductivity Group, Department of Electrical Engineering, Kyoto University, in 2019, as an Assistant Professor. His research interests include application of high  $T_c$  superconductors to magnets, evaluation of electromagnetic properties of high  $T_c$  superconducting coils and cables, and numerical analyses of high- $T_c$  superconducting coils and cables.

Dr. Sogabe was a Research Fellow of the Japan Society for the Promotion of Science, from 2016 to 2019. He received several awards equivalent to best presentation awards at international conferences on applied superconductivity, such as International Conference on Magnet Technology.



**RODNEY A. BADCOCK** (Senior Member, IEEE) has 32 years research experience in applied research and development covering manufacturing process monitoring and control, materials sensing, and superconducting systems. Since 2006, he has been concentrating on superconducting machines development, production, and excitation and control with the Paihau-Robinson Research Institute, Victoria University of Wellington, Lower Hutt, New Zealand. He is currently the Institute

Deputy Director, a Chief Engineer, and a Professor, and specializes in the management of complex engineering projects, including customer-focused multidisciplinary programmes. He is particularly known for the development of the superconducting dynamos for electric machines and the NZ MBIE programme developing aircraft superconducting electric propulsion technology. He is recognized as one of the leading experts in the application of superconducting dynamos, cables and protection to electric machines and translating high temperature superconductivity into commercial practice that has included General Cable Superconductors, Siemens, HTS-110, and several of the compact fusion programmes. Committed to the next generation, his Ph.D. students have gone on to achieve significant commercial success in their own right.

He was awarded the 2022 Royal Society Te Aparangi Pickering Medal for developing superconducting technologies that are enabling electrical machines at the leading edge of current engineering practice. He was a key member of the team awarded the Royal Society of New Zealand Cooper Medal, in 2008, for the development of high-temperature superconducting cables for power system applications, including one MVA transformer, 60 MW hydro generator, and 150 MW utility generator.



**JAMES G. STOREY** (Member, IEEE) was born in Hamilton, New Zealand, in 1979. He received the B.S. degree in physics and mathematics and the B.Sc. (Hons.) and Ph.D. degrees in physics from the Victoria University of Wellington, Wellington, New Zealand, in 2003, 2004, and 2007, respectively. From 2008 to 2011, he was a Research Associate with the Cavendish Laboratory, University of Cambridge, Cambridge, U.K. In 2011, he joined the Superconductivity Group currently

known as the Robinson Research Institute, Victoria University of Wellington, where he is currently a Senior Scientist. He is also a Principal Investigator with the MacDiarmid Institute for Advanced Materials and Nanotechnology, Wellington. His research interests include the electronic properties of high-temperature superconductors, superconducting levitation bearings, and electromagnetic finite-element modelling of superconducting machines. He is a member of the Institute of Physics, U.K., and the American Physical Society, USA.



**ZHENAN JIANG** (Senior Member, IEEE) received the B.Eng. degree in electrical engineering from Chongqing University, Chongqing, China, in 1994, and the M.Eng. and Ph.D.-Eng. degrees in applied superconductivity from Yokohama National University, Yokohama, Japan, in 2002 and 2005, respectively.

He was a Postdoctoral Research Fellow with Yokohama National University, from 2005 to 2008. He joined the Superconductivity Group currently known as the Robinson Research Institute, Victoria University of Wellington, New Zealand, in 2008, as a Research Scientist. He has a strong track record in characterization of high temperature superconductors (HTS), especially in AC loss. He is currently a Professor with the institute and leading AC loss research in the institute. His current research interests include AC loss characterization in HTS, HTS applications, including transformers, flux pumps, magnets, and rotating machines.

Prof. Jiang has been twice awarded the Japan Society for the Promotion of Science (JSPS) invitation fellowship to Kyoto University, in 2011 and 2015. Since 2021, he has become an Editorial Board Member of *Superconductivity* (Elsevier). He received the 2021 Scott Medal from the Royal Society of New Zealand, for his work on measuring and modelling the response of superconductors.

...